ADVANCED MATERIALS INTERFACES
Open Access
www.advmatinterfaces.de

Amplified Photoluminescence of $CsPbX_3$ Perovskites Confined in Silica Film with a Chiral Nematic Structure

*Marija Knezevic, Thi-Hieu Hoang, Cong Wang, Masa Johar, Alba Garzón Manjón, David Llorens Rauret, Christina Scheu, Marie Erard, David Berardan, Jordi Arbiol, Christophe Colbeau-Justin, and Mohamed Nawfal Ghazzal**

Metal halide perovskites (MHPs, CsPbX3: X = Cl, Br, I) have advanced the field of optoelectronic devices due to their remarkable light-emitting capabilities, stemming from the large overlap between their emission and absorption spectra, offering the possibility to reabsorb their own emitted photons. Herein, a straightforward method is reported to confine $CsPbBr_3$ into mesoporous silica films with a chiral nematic structure, allowing the amplification of the photoluminescence (PL). The simple room temperature ligand-free synthesis allows facile growth of $CsPbBr_3$ in silica photonic films, in which the Bragg peak position can be tuned from the UV to the visible range. The perovskite/silica films demonstrate a remarkable improvement in PL intensity and lifetime compared to the as-synthesized non-confined perovskite nanocrystals (NCs) due to the overlap of the Bragg peak position of the chiral nematic photonic films and $CsPbBr_3$ absorption band. Such a PL enhancement stems from the slow photon effect induced at blue and red Bragg peak edges that facilitates the photon recycling of the emitted photons. This innovative approach offers a new way to fabricate highly emissive and long-lived photoluminescent films at ambient conditions, potentially advancing perovskite utilization in light-emitting devices.

1. Introduction

MHPs have attracted ever-increasing attention for their application in light-harvesting materials.[1,2] MHPs exhibit remarkable charge transport properties,[3] long carrier lifetimes,[4] and low excitation binding energy.[5] Additionally, the electronic and optical properties are easily tuned by either controlling the chemical synthesis or selective substitution of the atoms, i.e., $CsPbBr_{3-y}X_y$ (X = Cl, I).[5] Compared to other semiconductors, MHPs exhibit unusual defect-tolerant photophysics,[6] which can be rationalized by the presence of defect energy levels localized either within the valence band (VB) or conduction band (CB) instead of being deep within the bandgap. Still, some defects, such as undesirable cation or anion vacancies, remain present, and their energy levels fall within the CB and VB, negatively affecting the PL properties. Several strategies have been proposed to advance the MHP-based emissive technology, significantly improving the photoluminescent quantum yield (PLQY).[7,8] Some suggested compositional engineering, crystal size tuning,(9) direct spin-coating of colloidal perovskite NCs,[10] constructing a quasi-core/shell structure that combines a high PLQY with balanced charge injection, surface passivation to reduce the charge trap density,[11] the introduction of functional molecules, metal ions, and halogen ions into the bulk or onto the surface of MHPs.[12]

Another paramount feature that has advanced MHPs in the field of optoelectronic devices, leading to their remarkable light-emitting capabilities, stems from the large overlap between their emission and absorption spectra, offering the possibility to reabsorb their own emitted photons, enhancing the PL intensity.

M. Knezevic, T.-H. Hoang, C. Wang, M. Johar, M. Erard, C. Colbeau-Justin, M. N. Ghazzal
Université Paris-Saclay
Institut de Chimie Physique
UMR 8000 CNRS, Orsay 91405, France
E-mail: mohamed-nawfal.ghazzal@universite-paris-saclay.fr

The ORCID identification number(s) for the author(s) of this article can be found under https://doi.org/10.1002/admi.202300636

DOI: 10.1002/admi.202300636

A. G. Manjón, D. L. Rauret, J. Arbiol
Catalan Institute of Nanoscience and Nanotechnology (ICN2)
CSIC and BIST
Campus UAB, Bellaterra, Barcelona 08193, Catalonia Spain

C. Scheu
Max-Planck-Institut für Eisenforschung GmbH
Max-Planck-Strasse 1, 402bu37 Düsseldorf, Germany

D. Berardan
ICMMO
UMR 8182 CNRS, Université Paris-Saclay, Orsay F-91405, France

J. Arbiol
ICREA
Pg. Lluís Companys 23, Barcelona 08010, Catalonia Spain

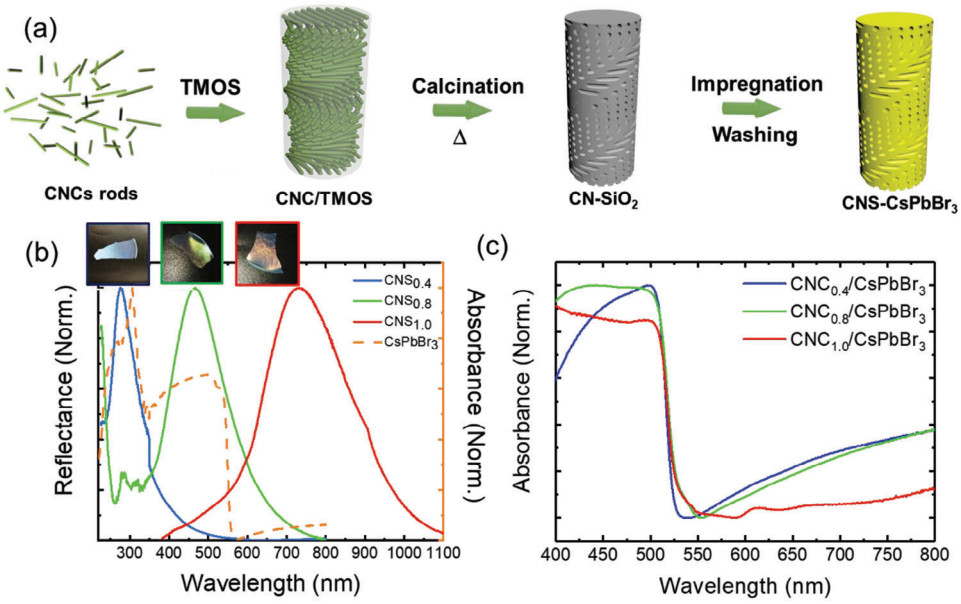

Figure 1. a) Schematic diagram of the template-synthesis of $CsPbBr_3$ confined in the mesoporous silica film with a chiral nematic structure. b) Images and reflectance spectra of silica films obtained with variable CNCs/TMOS ratio and diffuse reflectance spectrum of $CsPbBr_3$ NCs. c) Absorption spectra of $CNS_{0.4}/CsPbBr_3$, $CNS_{0.8}/CsPbBr_3$, and $CNS_{1.0}/CsPbBr_3$ films.

These properties make MHPs the primary choice material for next-generation color display applications.[13] An alternative to enhance the PL properties involves the photon recycling (PR) effect in textured films.[14,15] This process directly affects the PLQY since emitted photons undergo successive events involving the reabsorption of radiatively emitted photons, resulting in photogenerated charge recombination before eventually escaping from the film, enhancing the PL lifetime.[14,16] The PR process was only obtained by exploiting the light scattered at the film surface and interface structure.[14] Therefore, there is still a need to explore a substantially structured cavity and its effect on the PL of MHPs.

In this work, we developed a straightforward strategy enabling the confinement of MHPs in a periodically arranged mesoporous silica film, so-called photonic crystals (PCs). The aim is to improve the stability of MHP in an aqueous solution and simultaneously the quantum utilization of incident light. Up to now, mesoporous silica materials have been used to enhance the stability of MHPs and induce quantum confinement.[6,17,18] However, no attention has been paid to the effect of structuring the silica material on improving the PL of MHPs. The basics of the extraordinary properties of the PCs, which could be found in various species in nature, were proposed by Yablonovitch.[19,20] The PCs exhibit a photonic bandgap that inhibits light propagation when interacting with electromagnetic radiation (forbidden wavelength reflected by PCs). More importantly, the group velocity of light is expressed in Equation (1)

$$\vec{V}_g = \frac{\partial \omega}{\partial \vec{k}} \tag{1}$$

where ω the pulsation and k the wave vector, tends to zero near the blue and red edges of the photonic bandgap.[21] Slowing down the photons combined with the large overlap between the emission and absorption spectra of the MHPs is expected to maximize the PR (reabsorption–reemission events) and improve the PL intensity and lifetime.

As proof of our concept, we confined the low emissive MHPs into the mesoporous silica films with a chiral nematic structure using precipitation. Compared to the as-synthesized MHPs NCs, the $CsPbBr_3@SiO_2$ films demonstrate higher PL intensity and longer PL lifetime. More importantly, the improvement of PL properties matches the Bragg peak position of the chiral nematic photonic films, demonstrating the slow photon effect at their blue and red edges, facilitating the reabsorption of the emitted photons leading to the PL amplification of MHPs. This innovative approach provides an original way to fabricate highly emissive and long-lived photoluminescent films.

2. Results and Discussion

Cellulose nanocrystals (CNCs) are rod-like materials that can self-assemble into the chiral nematic structure during water evaporation and give rise to porous PCs after calcination (CNC removal) (**Figure 1**a).[22] The transfer of chiral nematic structure to the silica films after removing CNCs endows them with their unique chiral photonic properties. The pure chiral nematic silica (CNS) films show strong iridescent color and intense Bragg peak reflection. The wavelength maximum of the Bragg reflection was controlled by finely tuning the amount of tetramethyl orthosilicate (TMOS) in the stock solution (0.4–1 mL), labeled as $CNS_{0.4}$, $CNS_{0.8}$, and $CNS_{1.0}$. As the TMOS amount increases, the color of the films changes from blue to green to yellow, as revealed by UV–vis–NIR spectroscopy (Figure 1b). This corresponds to the red shift of the maximum wavelength of the Bragg reflection peak. The maximum wavelength reflected by the films (λ_{max}) is related to the effective refractive index "n_{eff}", the helical pitch "P",

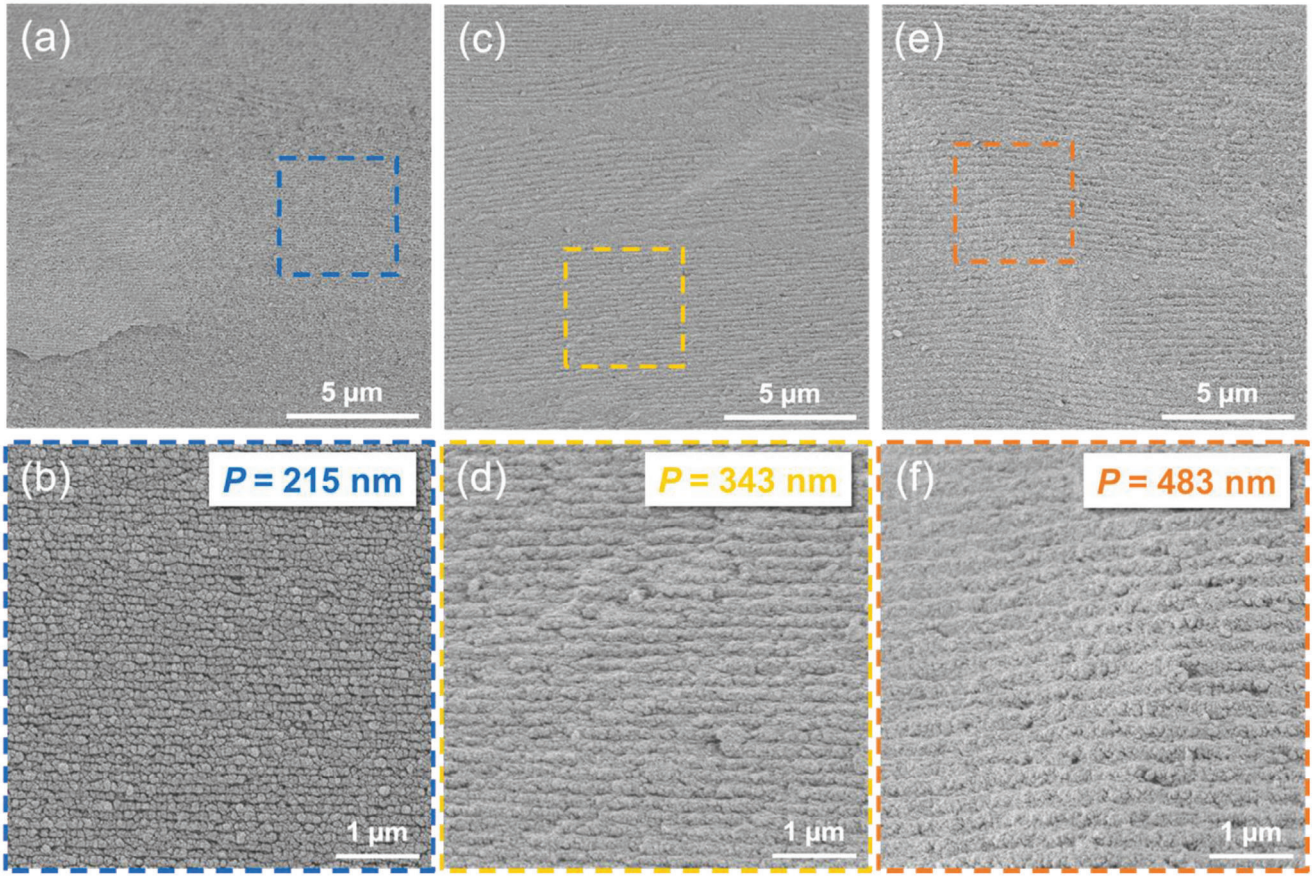

Figure 2. Cross-sectional images of a range of silica films obtained at different ratios of CNC/TMOS a,b) $CNS_{0.4}/CsPbBr_3$, c,d) $CNS_{0.8}/CsPbBr_3$, and e,f) $CNS_{1.0}/CsPbBr_3$.

and the angle between the film axis and the incident light, according to the following equation:[23]

$$\lambda_{max} = n_{eff} P \sin(\theta) \quad (2)$$

Assuming that the refractive index of CNS remains unchanged, the redshift arises from the pitch "*P*" increase.[24] This will be discussed further in the following morphological analysis of the film cross-section.

We synthesized low emissive cesium lead halide perovskite $CsPbBr_3$ NCs using a simple precipitation method at ambient conditions (Figure S1, Supporting Information). This method leads to almost phase-pure $CsPbBr_3$ NCs with only trace amounts of $CsPb_2Br_5$. $CsPbBr_3$ NCs display intense diffraction peaks corresponding to the well-crystallized orthorhombic $CsPbBr_3$ NCs (Figure S2, Supporting Information). Lattice parameters of $CsPbBr_3$ NCs were determined to be a = 8.2570 Å, b = 11.7629 Å, and c = 8.2121 Å (±0.001 Å). We used an identical method for confining $CsPbBr_3$ in the silica mesopores films, obtaining, $CNS_{0.4}/CsPbBr_3$, $CNS_{0.8}/CsPbBr_3$, and $CNS_{1.0}/CsPbBr_3$. We used UV–vis–NIR spectroscopy, scanning electron microscopy (SEM), high-resolution transmission electron microscopy (HRTEM), high-angle annular dark field scanning transmission electron microscopy (HAADF-STEM), and energy-dispersive X-ray spectroscopy (EDS) to deeply understand the optical, morphological, and compositional properties of the composite films. Figure 1c displays the UV–vis spectra of different silica films containing MHPs nanoparticles. A broad absorbance band was observed starting at 525 nm, typical of the direct optical bandgap of $CsPbBr_3$ perovskites. The bandgap of $CsPbBr_3$ NCs, $CNS_{0.4}/CsPbBr_3$, $CNS_{0.8}/CsPbBr_3$, and $CNS_{1.0}/CsPbBr_3$ films was estimated from the Kubelka–Munk modified function as 2.23, 2.37, 2.36, and 2.36 eV, respectively (Figure S3, Supporting Information). It is worth noting that the absorbance band edge of the MHPs confined in mesoporous silica films is blue-shifted for 0.13 eV. The observed shift indicates the downsizing of MHPs grown in the silica pores.

The SEM observations of the silica films cross-section obtained at different ratios of CNC/TMOS after calcination and MHPs confinement are shown in **Figure 2**. The films show layered morphology throughout their thickness, which is the typical fingerprint of the chiral nematic structure. The twist of the silica rods over a defined helical axe is further confirmed at higher magnification (Figure S4, Supporting Information). This demonstrates that the isotropic liquid crystalline organization of CNCs is successfully transferred into the inorganic silica films. It is worth noting that the pitch can be modified by controlling the concentration of the silica precursor, and an increase in the *P* is observed as the CNC/TMOS ratio increases. The average value of the *P* estimated from SEM images is 215, 343, and 483 nm for $CNS_{0.4}$,

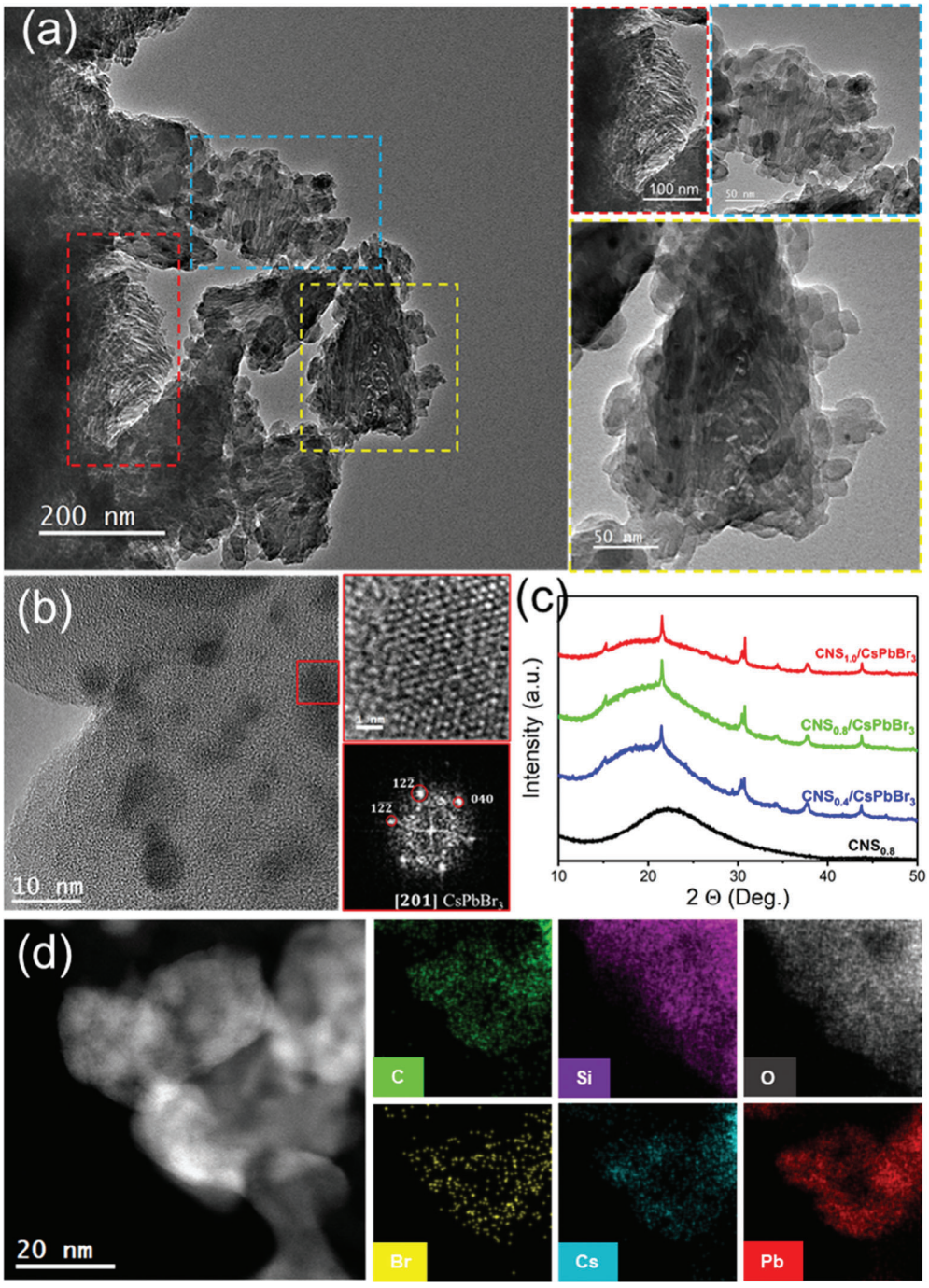

Figure 3. a) General view TEM images of $CNS_{0.8}/CsPbBr_3$, b) HRTEM image of spherical $CsPbBr_3$ NCs in $CNS_{0.4}$, and FFT of the squared area in red. The top right image is a magnified detail of the area in red. c) XRD patterns of CNS and CNS/MHP films. d) STEM-EDS compositional mapping of $CNS_{0.4}/CsPbBr_3$.

$CNS_{0.8}$, and $CNS_{1.0}$, respectively, which is consistent with the red-shift observed in the reflection spectra.

The morphology of the $CNS_{0.8}/CsPbBr_3$ film was further analyzed by TEM, and the results are shown in **Figure 3**a,b. The films are porous and exhibit locally aligned rods separated by mesopores. The localized fragments of silica rods appeared to be twisting around the helical axis perpendicular to the plane, confirming the chiral nematic organization of the photonic film. As estimated from the TEM images, the silica pore size has an average width of ≈8 nm, corresponding to the diameter of CNC rods, in agreement with reported studies.[24–26] Further investigations of the films by HR-TEM indicate the $CsPbBr_3$ inclusion in the film. Most of the nanoparticles are spherical (Figure 3b) and in the pore channels (Figures S5 and S6,

Table 1. Lattice parameters estimation of $CsPbBr_3$ nanoparticles grown in CNS films, obtained from XRD data.

Samples	a	b	c
$CNS_{0.4}/CsPbBr_3$	8.256	11.760	8.199
$CNS_{0.8}/CsPbBr_3$	8.261	11.763	8.202
$CNS_{1.0}/CsPbBr_3$	8.256	11.755	8.194

Supporting Information). The diffraction pattern obtained from FFT indicated crystalline $CsPbBr_3$. The average size distribution of spherical MHPs in $CNS_{0.8}/CsPbBr_3$ was estimated to be 6.7 ± 1.2 nm (Figure S7a, Supporting Information). The FFT diffraction pattern demonstrated crystalline $CsPbBr_3$. The mesoporous films behave as templates guiding the confined growth of perovskites, leading to the downsizing behavior. The morphology of the $CNS_{0.4}/CsPbBr_3$ is similar to the morphology of $CNS_{0.8}/CsPbBr_3$, with an average particle size of 6.7 ± 1.4 nm (Figure S7b, Supporting Information). Furthermore, we observed a limited amount of non-confined cubic $CsPbBr_3$ NCs on the surface of $CNS_{0.4}/CsPbBr_3$ and $CNS_{0.8}/CsPbBr_3$ films, with an average size of 28.3 ± 5.4 and 69.7 ± 11.4 nm, respectively. In $CNS_{1.0}/CsPbBr_3$ films, several spherical NPs were observed along the pores (Figure S8, Supporting Information); however, the surface of silica films is dominated by $CsPbBr_3$ nanocubes with an average size of 27.6 ± 6.7 nm.

The XRD patterns of silica mesopores photonic films containing MHPs nanoparticles ($CNS_{0.4}/CsPbBr_3$, $CNS_{0.8}/CsPbBr_3$, and $CNS_{1.0}/CsPbBr_3$) exhibit typical patterns of the orthorhombic $CsPbBr_3$, in agreement with HRTEM observations. In contrast, native silica film shows a broad band from 15° to 25°characteristic of the amorphous phase (Figure 3c). The lattice parameters of orthormobic $CsPbBr_3$ nanoparticles incorporated in CNS films are given in **Table 1**. A secondary phase due to a minor amount of unreacted CsBr was observed with a weak diffraction peak around 28.7°. The EDS mapping analysis (Figure 3d, Figure S9, Supporting information) confirmed the overlap of the silica mesoporous films with the localization Cs, Pb, and Br atoms, proving the formation of $CsPbBr_3$ nanoparticles inside the pores of CNS.

The optical properties of the photonic films with MHP nanoparticles were investigated, and the results are shown in **Figure 4**. The photographs of as-synthesized $CsPbBr_3$ NCs and $CNS/CsPbBr_3$ films are given in Figure 4a. To demonstrate the amplified emission we evaluated the steady-state and time-dependent PL performances of the $CsPbBr_3$ confined in films with a variable Bragg reflection wavelength maximum. Visual observations under daylight and under UV excitation (254 nm) indicate weak luminescence of the $CsPbBr_3$ powder. However, once the perovskite is confined into nanostructured CNS films, a bright emission is obtained for $CNS_{0.4}/CsPbBr_3$ and $CNS_{0.8}/CsPbBr_3$ films (Figure 4a). The spontaneous UV-activated PL decreases significantly for $CNS_{1.0}/CsPbBr_3$. These observations were confirmed by steady-state PL spectroscopy measurements (Figure 4b). A remarkable increase in PL intensity is observed, up to ten fold,[when the amount of silica precursor increases, reaching its maximal value for $CNS_{0.8}/CsPbBr_3$. In addition, the maximum wavelength is red-shifted to 519 nm. Such a redshift, also observed for perovskite assembled into 2D photonic supercrystals,[27] underlines a strong degree of coupling phenomenon between confined MHPs nanoparticles, amplified by the silica photonic structure and the slow photon effect. A further increase in the amount of silica leads to the redshift of the Bragg peak maximum to a higher wavelength and results in a quenched PL intensity. The PL lifetime was probed by time-resolved fluorescence lifetime imaging (TRPL) at 440 nm excitation. The PL imaging demonstrated a significant change in the PL decay upon embedding MHP in the photonic films (Figure 4c). The PL lifetime was remarkably enhanced when MHPs were grown into silica films with photonic properties. The PL lifetime is remarkably improved in the case of $CNS_{0.4}$ and $CNS_{0.8}$. It is four times higher compared to the solely $CsPbBr_3$ NCs due to the significant overlap between the blue ($CNS_{0.4}$) and red edge of the Bragg peak ($CNS_{0.8}$), and $CsPbBr_3$ absorption spectral line (7.8 and 8.4 ns for $CNS_{0.4}/CsPbBr_3$ and $CNS_{0.8}/CsPbBr_3$, respectively) (**Table 2**). However, the PL average lifetime increases from 2.8 ns for $CsPbBr_3$ NCs to 3.1 ns for $CNS_{1.0}/CsPbBr_3$ films. Such a nonsignificant PL improvement stems from the mismatch between $CNS_{1.0}$ blue-edge of the Bragg peak and $CsPbBr_3$ absorption. The enhanced and long-lived PL of MHPs confined in CNS films relies on the photonic bandgap position. The absorbance band of MHPs coincides with the blue edge of the Bragg peak position of $CNS_{0.8}$ and the red edge of the Bragg peak of $CNS_{0.4}$ film. The perfect match between the absorbance band of the MHPs and the blue and red edge of the silica PC promotes the light scattering inside the films, slowing the speed of light. This paramount feature increases the photon retention inside the structure and the perovskite absorbance factor. In other words, MHPs have more time to absorb photons, lowering the number of non-absorbed photons. As a photon is emitted from the MHPs, it experiences a slow photon itself, since the emission wavelength matches with either the blue or red edge of the photonic gap while being trapped in the photonic cavity. The surrounding MHP nanoparticles can reabsorb the emitted light, leading to the multiple reabsorption/reemission processes before leaving the film (Figure 4d). Such a phenomenon has been recently demonstrated in surface-structured MHPs films.[28] As the Bragg position is shifted to a higher wavelength, the range of these edges no longer matches the absorbance band of MHPs leaving only a limited effect on the PL intensity and lifetime. In addition, since MHPs exhibit large overlaps between their emission and absorption spectra, reabsorption of the emitted light is expected to occur and induce PR.

The films, kept without further protection, were exposed to the ambient environment at room temperature for 30 days, and a daily PL intensity was measured to assess their stability (Figure 4e). PL intensity starts decreasing for $CNS_{0.8}/CsPbBr_3$ compared to $CNS_{0.4}/CsPbBr_3$, while the PL intensity for the $CNS_{1.0}/CsPbBr_3$ film remains low but relatively stable over time. The PL properties of confined MHPs showed remarkable stability over time under an ambient atmosphere, with high PL intensity, due to the limited chemical interaction with ambient oxygen and moisture.[29] It is known that $CsPbBr_3$ NCs are very sensitive to moisture that makes them susceptible to degradation and PL quenching.[30] To preserve long-term high emission intensity, we grafted a hydrophobic layer of fluorinated alkyl silane, i.e., tridecafluorooctyl triethoxysilane (FAS) at the

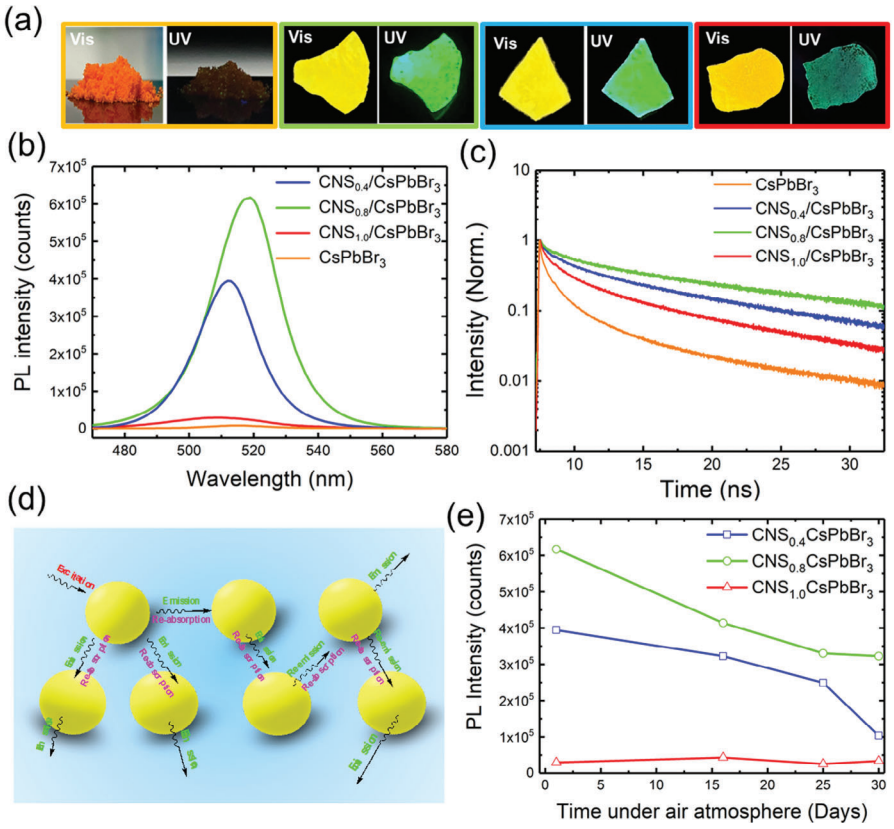

Figure 4. a) From left to right, photographs under ambient and UV illumination of non-confined $CsPbBr_3$ NCs and $CNS_{0.4}/CsPbBr_3$, $CNS_{0.8}/CsPbBr_3$, and $CNS_{1.0}/CsPbBr_3$ films. b) Emission spectra of $CNS_{0.4}/CsPbBr_3$, $CNS_{0.8}/CsPbBr_3$, and $CNS_{1.0}/CsPbBr_3$. c) TRPL lifetime decays obtained at 440 nm excitation. d) Schematic representation of PR in the CNS films containing $CsPbBr_3$ NCs. e) PL evolution over time under ambient atmosphere.

surface of $CNS_{0.8}/CsPbBr_3$ films to improve their stability against moisture. Upon immersion of $CNS_{0.8}/CsPbBr_3$ films in water, it demonstrated a color change of the sample due to water infiltration into the porous silica structure and the modification of the refractive index of the surrounding media, with blue substantial luminescence followed by immediate PL quenching and structural degradation. The grafting of FAS hydrophobic molecule allows the film to maintain its greenish PL, attesting to the inhibition of water diffusion into the films (Figure S10, Supporting Information).

To extend our study to the broader spectral range, we investigated MHPs optical properties upon anion substitution. Interestingly, our room temperature synthesis resulted in both luminescent $CNS_{0.8}/CsPbBr_{3-y}Cl_y$ and $CNS_{0.8}/CsPbBr_{3-y}I_y$ films upon 5-min-long immersion in PbX_2 concentrated solution (X = Cl, I) (**Figure 5**a). The anion-exchange process gives a simple substitutional technique to modify the composition and emission position in visible spectrum areas perceptible to the human eye.[31] The bandgap of $CNS_{0.8}/CsPbBr_{3-y}Cl_y$ and $CNS_{0.8}/CsPbBr_{3-y}I_y$ films were estimated from the Kubelka–Munk modified function to be 2.7 and 2.2 eV, respectively (Figure S11, Supporting Information). However, the mixed halide films demonstrate an emission band of ≈520 nm, which can be explained by halide migration and incomplete substitution of bromide. It is possible to control the rate of anion substitution by immersing films in a concentrated solution of PbX_2 (X = Cl, I) during different time intervals (5–30 min), resulting in the bandgap tuning, with emission maximum ranging from 450 to 580 nm (Figure S12a, Supporting Information). Under ambient conditions, the anion-exchanged films kept identical color for more than a month unless being ground. Nevertheless, the XRD patterns of these samples could not provide clear phase distinction due to substantial amorphous phase contribution. It seems that $CNS_{0.8}/CsPbBr_{3-y}I_y$ consists of mixed Br/I orthorhombic perovskite; however, small and broad peaks cannot be resolved with sufficient certainty. Interestingly, complete anion substitution with PbI_2 resulted in yellow nonluminescent films. Further investigation of anion substitution with Cl demonstrated dramatic structural modification, i.e., $CNS_{0.8}/CsPbBr_{3-y}Cl_y$ predominantly consists of an unknown non-perovskite phase, which could correspond to $CsPb_2Cl_5$, since longer immersion for up to 30 min, results in the predominant $CsPb_2Cl_5$ non-perovskite phase (Figure S12b, Supporting Information). The presence of iodide and chloride was also confirmed by EDS (Figures S13–S15, Supporting Information). Consequently, TRPL revealed considerable fluorescence quenching upon anion substitution of bromide with iodide and chloride (Figure 5b). The average lifetime decreased to 0.78 and 0.75 ns for $CNS_{0.8}/CsPbBr_{3-y}Cl_y$ and $CNS_{0.8}/CsPbBr_{3-y}I_y$, respectively. Upon anion substitution, the contribution of short kinetic components (τ_3) becomes significant (Table S1, Supporting Information). The contribution of τ_4 cannot be assigned with certainty since the instrument response function is of the same order of magnitude.

Table 2. The PL multiexponential lifetime decays with decay fractions of $CNS_{0.4}/CsPbBr_3$, $CNS_{0.8}/CsPbBr_3$, $CNS_{1.0}/CsPbBr_3$, and $CsPbBr_3$ nanopowder.

Samples	τ_1 [ns]	τ_2 [ns]	τ_3 [ns]	$\tau_{average}$ [ns]
$CNS_{0.4}/CsPbBr_3$	14 ± 0.3	2.8 ± 0.1	0.46 ± 0.02	7.8 ± 0.1
51%	24%	25%		
$CNS_{0.8}/CsPbBr_3$	18 ± 0.8	3.8 ± 0.1	0.46 ± 0.01	8.4± 0.3
40%	30%	30%		
$CNS_{1.0}/CsPbBr_3$	9.9 ± 0.6	2.4 ± 0.1	0.41 ± 0.01	3.1 ±0.1
22%	32%	46%		
$CsPbBr_3$	9.2 ± 0.9	1.5 ± 0.3	0.25 ± 0.3	2.8 ± 0.2
25%	25%	50%		

The anion substitution introduces trapping centers that result in dominant non-radiative decay paths, leading to significant PL quenching. These results demonstrate the possibility of a room-temperature anion substitution in $CNS_{0.8}/CsPbBr_3$ films. However, further studies are necessary to improve their crystallinity, PL lifetime, and the optimization of optical bandgap overlap with the photonic bandgap of CNS films.

3. Conclusion

A series of $CNS_x/CsPbBr_3$ (x = 0.4, 0.8, 1.0) photonic films were successfully synthesized using an evaporation-induced self-assembly process and precipitation method. The results show that $CNS_x/CsPbBr_3$ films displayed extraordinary bright green fluorescence. Owing to the significant overlap of $CsPbBr_3$ absorption spectral lines and $CNS_{0.8}$ ($CNS_{0.4}$) blue (red) photonic edge, a slow photonic effect was induced that directly influenced PL through the PR effect, together with the downsizing effect of $CsPbBr_3$ within CNS pores. Such heterostructure experiences quite good stability under ambient conditions, while coating with a hydrophobic molecular layer allows direct immersion of $CNS_x/CsPbBr_3$ in water, demonstrating ephemeral PL. Using textured active films is an inexpensive way of synthesizing highly luminescent quantum-confined $CsPbBr_3$ NCs that could improve PL for photonic and light-emitting applications. Incorporating $CsPbBr_3$ into the photonic films with a chiral nematic structure is a step forward in generating highly luminescent materials. Further developments are needed to incorporate $CNS_x/CsPbBr_3$ in a white light-emitting diode and improve their stability in harsh media and at higher temperatures. In addition, the synthesis optimization of mixed halide perovskites, i.e., $CsPbBr_{3-y}I_y$ and $CsPbBr_{3-y}Cl_y$, incorporated in CNS films, with improved structural and optical properties, would offer more flexibility in PL coloration of the films.

4. Experimental Section

Materials: Lead iodide (PbI_2, ≥99.0%), lead chloride ($PbCl_2$, ≥99.0%), and lead bromide ($PbBr_2$, ≥98.0%) were purchased from Acros Organic. Cesium bromide (CsBr, 99%) was purchased from Alfa Aesar, while dimethyl sulfoxide (DMSO, ≥99.0%), toluene (99.8%), hexane (95%), and TMOS (≥99.0%) were purchased from Sigma–Aldrich. CNCs (purchased from the University of MAINE) were used without further purification. All chemicals used were analytical grade and were directly used without further purification.

Elaboration of SiO_2 Photonic Films with a Chiral Nematic Structure: The procedure used for the film elaboration was adapted from previously reported methods.[22,25] Adequate amount (0.4, 0.8, and 1.0 mL) of TMOS was added to 5.0 mL CNCs aqueous suspension (4 wt%, pH = 2.4) previously sonicated during 1 h in glass vials. The suspension was stirred for 15 min at room temperature. Subsequently, the CNCs/TMOS mixtures were transferred to polystyrene petri dishes and left to dry at room temperature without any control of the environment atmosphere. CNC/silica hybrid films with different colors and helical pitch values were obtained after 24 h. The biotemplate (CNCs) was removed by calcination under air at 540 °C for 4 h at a heating rate of 2 °C min^{-1} to generate mesopores CNSs films.

Synthesis of CNS/$CsPbBr_3$ Films: $CsPbBr_3$ precursor solution was prepared by dissolving 0.4 mmol $PbBr_2$ and 0.4 mmol CsBr in 1 mL DMSO under sonication for 1 h. Then, the silica films with controlled photonic properties ($CNS_{0.4}$, $CNS_{0.8}$, and $CNS_{1.0}$) were immersed in-stock solution for 12 h at ambient conditions. Subsequently, CNS/$CsPbBr_3$ films were taken out, washed several times with toluene and hexane, and dried at room temperature, yielding $CNS_{0.4}/CsPbBr_3$, $CNS_{0.8}/CsPbBr_3$, and $CNS_{1.0}/CsPbBr_3$ films. In comparison, $CsPbBr_3$ NCs were obtained following the identical procedure. The equimolar amount (0.4 mmol) of $PbBr_2$ and CsBr was mixed and dissolved in DMSO (1 mL). The obtained solution was drop-cast on a glass and dried under ambient conditions. Upon evaporation of DMSO, $CsPbBr_3$ NCs were formed, collected, and ground.

Synthesis of CNS/$CsPbBr_{3-y}X_y$ (X = Cl, I) Hybrid Films: The anion substitution is achieved by a simple partial exchange of Br atom with Cl and I atoms. Stock solutions of $PbCl_2$ and PbI_2 were prepared by dissolving 0.4 mmol $PbCl_2$ and 0.4 mmol PbI_2 in 1 mL DMSO

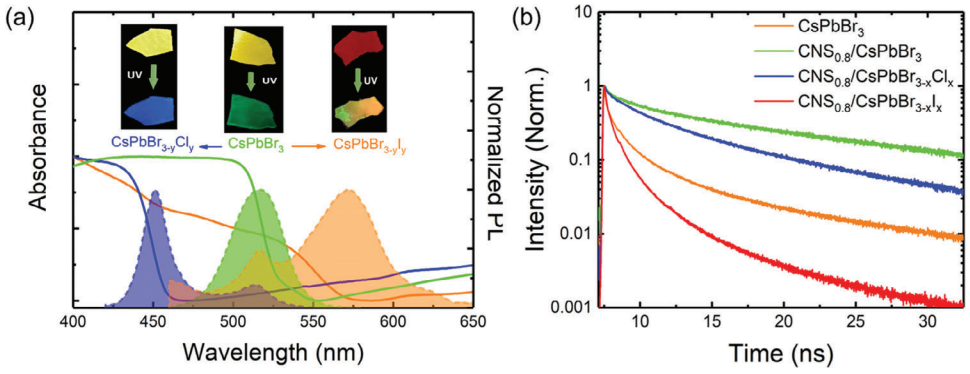

Figure 5. a) Absorption and emission spectra of $CNS_{0.8}/CsPbBr_{3-y}X_y$ (X = Cl, I) with their corresponding sample photographs under ambient and UV illumination. b) TRPL lifetime decays of $CsPbBr_3$ nanopowder, $CNS_{0.8}/CsPbBr_3$, $CNS_{0.8}/CsPbBr_{3-y}Cl_y$, and $CNS_{0.8}/CsPbBr_{3-y}I_y$ films.

under sonication for 1 h. Previously prepared film CNC/$CsPbBr_3$ was directly immersed in a solution of either PbI_2 (0.4 mmol) or $PbCl_2$ (0.4 mmol) stock solution, and the substitution rate was controlled by immersion time (30 min). After anion substitution, films were taken out, washed several times with toluene and hexane, and dried at room temperature.

Synthesis of $CNS_{0.8}$/$CsPbBr_3$ Films Coated with Hydrophobic Molecular Layer: A solution of tridecafluorooctyl triethoxysilane (FAS) was prepared by dissolving FAS (200 µL) in hexane (800 µL). $CNS_{0.8}$/$CsPbBr_3$ films were immersed in the as-prepared solution for 2 h. After drying, the stability of the films was evaluated by immersing films in pure water.

Characterization Techniques: Diffusion reflectance spectra (DRS) were recorded using UV–vis–NIR Cary 5000 UV–vis–NIR spectrophotometer (Agilent Technologies), equipped with an integrating sphere for diffuse and total reflection measurements. The maximum reflectance was set to 100% using $BaSO_4$ as a reference in the 200–1100 nm wavelength range.

The PL emission spectra were recorded using Fluorolog 3 HORIBA fluorimeter equipped with a solid sample holder. All samples were excited at 400 nm, and emission was monitored in the 450–700 nm range.

X-ray diffraction (XRD) measurements were carried out by room temperature powder X-ray diffraction (P-XRD). Patterns were recorded by a Panalytical X'Pert diffractometer with a Ge (111) incident monochromator (Cu Kα radiation) and an X'celerator detector.

The scanning electron microscopy (SEM) cross-section images were acquired with a ZEISS Supra 55VP FEG-SEM with an operating voltage of 2 kV and a working distance of 3–5.7 mm.

Transmission electron microscopy (TEM). The TEM images were obtained using a JEOL JEM 2100Plus, operating at 200 kV, and a Tecnai F20 field emission gun (FEG) microscope at 200 kV. The size of synthesized nanostructures was determined by Gatan Digital Micrograph software. The samples were crashed in small pieces, dispersed in hexane by stirring and deposited on the lacey carbon grids. The sonication was avoided for the grid preparation to limit the degradation/dissolution of perovskites. The perovskite can be destroyed under the beam and during the image acquisition. Therefore, the acquisition time is only less than 10 min.

The high-angle annular dark field scanning TEM (HAADF-STEM). TEM analysis was conducted using a Titan Themis 60-300 X-FEG microscope from Thermo Fischer Scientific. The microscope was equipped with a probe corrector and was operated at 300 kV. High-angle annular dark field (HAADF) images, with an angular range of 72–352 mrad, and EDS measurements were obtained using scanning transmission electron microscopy (STEM). The HAADF images were acquired with a current of ≈100 pA, while the EDS measurements utilized a current of around 150 pA. The STEM setup included a convergence semi-angle of ≈23.8 mrad and a beam size of roughly 0.1 nm. Moreover, STEM images have been analyzed by Gatan Digital Micrograph software and EDS data with Bruker ESPRIT software. To emphasize the lattice planes in the HRTEM images, we applied frequency mask filters and added the filtered image to the original.

Time-correlated single-photon counting (TCSPC) microscopy was performed by a homemade setup with a TE2000 microscope equipped with a 60 × 1.2NA water immersion objective (Nikon). The pulsed excitation source was an LDH 440 nm pulsed diode (80 ps FWHM, 10 MHz of repetition rate, PicoQuant). Lifetime measurements were analyzed by the Pico-Quant SymPhoTime software (v5.3.2), which calculates the intensity image of the observed field of view. The TCSPC fluorescence decay of a chosen ROI was calculated by SymPhotTime and exported for further analysis.[32]

Supporting Information

Supporting Information is available from the Wiley Online Library or from the author.

Acknowledgements

MK acknowledges the French « Ministère de l'enseignement supérieur et de la recherche» (MESR) for the PhD grant. MNG thanks the public grant overseen by the French National Research Agency (ANR), through the IngenCat project (ANR-20-CE43-0014) and NEXTCCUS project as part of the ERANET-ACT3 call program for the financial support. The authors thank F. Brisset for his valuable help in performing SEM and TEM analysis. ICN2 is supported by the Severo Ochoa program from Spanish MCIN / AEI (Grant no.: CEX2021-001214-S) and is funded by the CERCA Programme from the Generalitat de Catalunya. ICN2 acknowledges funding from Generalitat de Catalunya 2021SGR00457. MCIN supported this study with funding from European Union NextGenerationEU (PRTR-C17.I1) and Generalitat de Catalunya. The authors thank the support from the project NANOGEN (PID2020-116093RB-C43), funded by MCIN/ AEI/10.13039/501100011033/ and by "ERDF A way of making Europe," by the "European Union." AGM acknowledges the RyC Programme by MCIN/AEI and Ayuda RYC2021-033479- I financiada por MCIN/AEI /10.13039/501100011033 y por la Unión Europea NextGenerationEU/PRTR.

Conflict of Interest

The authors declare no conflict of interest.

Data Availability Statement

The data that support the findings of this study are available from the corresponding author upon reasonable request.

Keywords

chiral nematic silica, perovskites, photoluminescence, photon recycling

Received: July 26, 2023
Revised: September 28, 2023
Published online:

[1] K. Lin, J. Xing, L. N. Quan, F. P. G. De Arquer, X. Gong, J. Lu, L. Xie, W. Zhao, D. Zhang, C. Yan, W. Li, X. Liu, Y. Lu, J. Kirman, E. H. Sargent, Q. Xiong, Z. Wei, *Nature* **2018**, *562*, 245.
[2] S.-H. Jeong, J. Park, T.-H. Han, F. Zhang, K. Zhu, J. S. Kim, M.-H. Park, M. O. Reese, S. Yoo, T.-W. Lee, *Joule* **2020**, *4*, 1206.
[3] S. Zhou, R. Tang, L. Yin, *Adv. Mater.* **2017**, *29*, 1703682.
[4] S. Schünemann, S. Brittman, K. Chen, E. C. Garnett, H. Tüysüz, https://doi.org/10.1021/acsphotonics.7b00780.
[5] J. Shamsi, A. S. Urban, M. Imran, L. De Trizio, L. Manna, *Chem. Rev.* **2019**, *119*, 3296.
[6] D. N. Dirin, L. Protesescu, D. Trummer, I. V. Kochetygov, S. Yakunin, F. Krumeich, N. P. Stadie, M. V. Kovalenko, *Nano Lett.* **2016**, *16*, 5866.
[7] W. Xu, Q. Hu, S. Bai, C. Bao, Y. Miao, Z. Yuan, T. Borzda, A. J. Barker, E. Tyukalova, Z. Hu, M. Kawecki, H. Wang, Z. Yan, X. Liu, X. Shi, K. Uvdal, M. Fahlman, W. Zhang, M. Duchamp, J.-M. Liu, A. Petrozza, J. Wang, L.-M. Liu, W. Huang, F. Gao, *Nat. Photonics* **2019**, *13*, 418.
[8] L. Zhang, X. Yang, Q. Jiang, P. Wang, Z. Yin, X. Zhang, H. Tan, Y. M. Yang, M. Wei, B. R. Sutherland, E. H. Sargent, J. You, *Nat. Commun.* **2017**, *8*, 15640.
[9] X. Li, Y. Wu, S. Zhang, B. Cai, Y. Gu, J. Song, H. Zeng, *Adv. Funct. Mater.* **2016**, *26*, 2435.
[10] Y.-H. Kim, C. Wolf, Y.-T. Kim, H. Cho, W. Kwon, S. Do, A. Sadhanala, C. G. Park, S.-W. Rhee, S. H. Im, R. H. Friend, T.-W. Lee, *ACS Nano* **2017**, *11*, 6586.

[11] L. Huang, Z. Ge, X. Zhang, Y. Zhu, *J. Mater. Chem. A* **2021**, *9*, 4379.
[12] E. Aydin, M. De Bastiani, S. De Wolf, *Adv. Mater.* **2019**, *31*, 1900428.
[13] X. Zhao, J. D. A. Ng, R. H. Friend, Z.-K. Tan, *ACS Photonics* **2018**, *5*, 3866.
[14] J. M. Richter, M. Abdi-Jalebi, A. Sadhanala, M. Tabachnyk, J. P. H. Rivett, L. M. Pazos-Outón, K. C. Gödel, M. Price, F. Deschler, R. H. Friend.
[15] L. M. Pazos-Outón, M. Szumilo, R. Lamboll, J. M. Richter, M. Crespo-Quesada, M. Abdi-Jalebi, H. J. Beeson, M. Vrucinic, M. Alsari, H. J. Snaith, B. Ehrler, R. H. Friend, F. Deschler, *Science* **2016**, *351*, 1430.
[16] D. W. Dequilettes, K. Frohna, D. Emin, T. Kirchartz, V. Bulovic, D. S. Ginger, S. D. Stranks, *Chem. Rev.* **2019**, *119*, 11007.
[17] V. Malgras, S. Tominaka, J. W. Ryan, J. Henzie, T. Takei, K. Ohara, Y. Yamauchi, *J. Am. Chem. Soc.* **2016**, *138*, 13874.
[18] M. N. An, S. Park, R. Brescia, M. Lutfullin, L. Sinatra, O. M. Bakr, L. De Trizio, L. Manna, *ACS Energy Lett.* **2021**, *6*, 900.
[19] E. Yablonovitch, *Phys. Rev. Lett.* **1987**, *58*, 2059.
[20] G. S. Zhang, Z. Q. Huang, *Opt. Express* **2010**, *18*, 13361.
[21] P. Vukusic, J. R. Sambles, *Bionanotechnol* **2020**, *424*, 516.
[22] K. E. Shopsowitz, H. Qi, W. Y. Hamad, M. J. Maclachlan, *Nature* **2010**, *468*, 422.
[23] H. de Vries, *Acta Crystallogr.* **1951**, *4*, 219.
[24] C. Wang, J. Li, E. Paineau, A. Laachachi, C. Colbeau-Justin, H. Remita, M. N. Ghazzal, *J. Mater. Chem. A* **2020**, *8*, 10779.
[25] K. E. Shopsowitz, J. A. Kelly, W. Y. Hamad, M. J. Maclachlan, *Adv. Funct. Mater.* **2014**, *24*, 327.
[26] G. D. Gesesse, C. Li, E. Paineau, Y. Habibi, H. Remita, C. Colbeau-Justin, M. N. Ghazzal, *Chem. Mater* **2019**, *31*, 4851.
[27] D. Vila-Liarte, M. W. Feil, A. Manzi, J. L. Garcia-Pomar, H.e Huang, M. Döblinger, L. M. Liz-Marzán, J. Feldmann, L. Polavarapu, A. Mihi, *Angew. Chem., Int. Ed.* **2020**, *59*, 17750.
[28] C. Cho, B. Zhao, G. D. Tainter, J.-Y. Lee, R. H. Friend, D. Di, F. Deschler, N. C. Greenham, *Nat. Commun.* **2020**, *11*, 611.
[29] S. Chen, A. Nurmikko, *ACS Photonics* **2017**, *4*, 2486.
[30] X. Lu, Y. Hu, J. Guo, C.-F. Wang, S.u Chen, *Adv. Sci.*, https://doi.org/10.1002/advs.201901694.
[31] S.-M. Kang, B. Park, G. S. R. Raju, S. Baek, S. K. Hussain, C. H. Kwak, Y.-K. Han, J. S. Yu, S.-W. Kim, Y. S. Huh, *Chem. Eng. J.* **2020**, *384*, 123316.
[32] M. Erard, A. Fredj, H. Pasquier, D.-B. Beltolngar, Y. Bousmah, V. Derrien, P. Vincent, F. Merola, *Mol. BioSyst.* **2013**, *9*, 258.